MIMOSA: An Automatic Change Detection Method for SAR Time Series

Guillaume Quin, Béatrice Pinel-Puysségur, Jean-Marie Nicolas, and Philippe Loreaux

***Abstract*—This paper presents a new automatic change detection technique for synthetic aperture radar (SAR) time series, i.e., Method for generalIzed Means Ordered Series Analysis (MIMOSA). The method compares only two different temporal means between the amplitude images, whatever the length of the time series. The method involves three different steps: 1) estimation of the amplitude distribution parameters over the images; 2) computation of the theoretical joint probability density function between the two temporal means; and 3) automatic thresholding according to a given false alarm rate, which is the only change detection parameter. The procedure is executed with a very low computational cost and does not require any spatial speckle filtering. Indeed, the full image resolution is used. Due to the temporal means, the data volume to process is reduced, which is very helpful. Moreover, the two means can be simply updated using the new incoming images only. Thus, the full time series is not processed again. Change detection results between image pairs are presented with the airborne sensor CARABAS-II, using a public data release, and with TerraSAR-X data. In the case of time series, change detection results are illustrated using a TerraSAR-X time series. In every case, the MIMOSA method produces very good results.**

***Index Terms*—Change detection, Method for generalIzed Means Ordered Series Analysis (MIMOSA), synthetic aperture radar (SAR).**

I. Introduction

THE detection of changes on Earth is an important application of remote sensing. We can cite many applications for change detection using satellites or airborne sensors, such as environmental monitoring [1], [2], the observation of natural disasters [3]–[5], or the study of changes due to human activity [6], [7]. In this context, synthetic aperture radar (SAR) sensors present several advantages compared with optical sensors. First, the SAR sensors can be used during the day and during the night. Second, the scene of interest is not masked by clouds, which is a major problem for optical acquisitions. Because of these two main advantages, the SAR images are sometimes the only useful data during crisis to organize emergency rescue. Moreover, due to new satellite constellations such as COSMO–SkyMed, it is now possible to quickly obtain large time series over an area. The proposed change detection method reduces the data volume to process, using only two temporal means whatever the length of the time series. Indeed, we will see that the temporal means enable to deal with large time series at a very low computational cost, as well as to easily take into account a new incoming image.

Usually, change detection using repeat–pass SAR data involves the analysis of two coregistered images acquired over the same area of interest. Two main approaches have been developed in the literature to solve this problem. The first approach is called coherent change detection: It uses the phase information contained in the SAR images through the study of the coherence map [8]. The second approach, which can be qualified of incoherent change detection, only compares the amplitudes of the SAR images, as in the proposed method.

Several change detection techniques dedicated to SAR amplitude images are described in the literature. A well-known operator is the log–ratio between two SAR amplitude images [9]. After a speckle noise reduction step, the log–ratio image is thresholded in order to detect changes. To improve this technique, some automatic thresholding methods have been developed [10]. Multiscale analysis with the log–ratio image [11] enhances change detection and deals with heterogeneous data. Moreover, the log–ratio detector has been also adapted to fuzzy hidden Markov chains [12]. The first main advantage of the log–ratio operator is its computational simplicity. The second advantage is that automatic thresholding methods exist. Nevertheless, the two amplitude images used to compute the log–ratio need to be spatially filtered in order to reduce the speckle noise, which causes a loss of resolution. Without this prior spatial filtering, the log–ratio image is very noisy and direct thresholding generates a high number of false detections. Thus, a drawback of this technique is that the information contained in the amplitude data could be destroyed during the prior spatial filtering step if the filter is not well adapted. A second drawback is that only two images can be compared. Thus, the log–ratio operator is not directly adapted to deal with time series.

The maximum likelihood approach has been adapted to the detection of radar cross-section fluctuations through SAR time series [13]. For this purpose, the ratio between the geometric and the arithmetic temporal means of the amplitude time series is computed. This statistical test, called generalized likelihood ratio test (GLRT), is then thresholded in order to detect changes. The proposed method also uses temporal means but in a different and more accomplished way than the thresholding of the GLRT. We can mention that another maximum likelihood approach has been also developed for the detection of step patterns in the amplitude profiles of time series [14].

Manuscript received September 5, 2012; revised January 29, 2013, June 4, 2013, and September 25, 2013; accepted October 15, 2013.

G. Quin, B. Pinel-Puysségur, and P. Loreaux are with the Commissariat à l'Énergie Atomique et aux Énergies Alternatives (CEA), Direction des Applications Militaires Île-de-France (DAM DIF), 91297 Arpajon, France.

J.-M. Nicolas is with the École Nationale Supérieure des Télécommunications (Télécom ParisTech), 75013 Paris, France.

Color versions of one or more of the figures in this paper are available online at http://ieeexplore.ieee.org.

Digital Object Identifier 10.1109/TGRS.2013.2288271

Another technique to deal with SAR time series is the application of the log cumulants to detect spatiotemporal discontinuities [15]. For this purpose, the log cumulants are computed over spatiotemporal neighborhoods in order to estimate the statistical distribution parameters in the considered voxel. Two kinds of discontinuities are then detected simultaneously, namely, the stable spatial features and the temporal changes. Thus, the main drawback of this technique is that the interpretation of the results may be very difficult because these two pieces of information are merged.

A statistical similarity measure can be also used to detect changes along SAR time series [16]. In this technique, the temporal evolution of the local statistics is studied along the time series using the Kullback–Leibler (KL) divergence. The temporal changes are then related to the evolution of the local statistics between the different images, through very few statistical parameters, which are estimated at a very low computational cost. The main drawback of this technique is that spatial neighborhoods are used to estimate the local statistical parameters. Thus, the resolution of the change map is lower than the original resolution. It is thus very difficult to detect small punctual changes because of the loss of resolution. A different statistical method involves bivariate gamma distributions (BGDs) [17], [18] (which are simple multivariate distributions [19]) between image pairs using the mutual information between the amplitude images in order to detect the changes.

Information theoretic concepts have been also adapted to the problem of change detection between two SAR images [20]–[22]. This change feature is inspired by a heterogeneity indicator [23] through the study of scatterplots between the two considered amplitude images (equivalent to 2-D histograms). The proposed method also uses scatterplots to detect the changes but in a more accomplished way.

The change detection principle presented in this paper was first briefly described in [24], only focused on the case of SAR image pairs. In this paper, the Method for generalIzed Means Ordered Series Analysis (MIMOSA) change detection method is detailed in the case of SAR image pairs and time series.

This paper is organized as follows. First, the problem is formulated through the definition of the generalized temporal means, where a general description of the method is proposed. Then, the automatic change detection procedure is separately detailed in the two different cases of image pairs and time series. Finally, change detection results are presented between SAR image pairs with CARABAS-II airborne data and TerraSAR-X Stripmap descending data. The change detection results along SAR time series are also presented using TerraSAR-X Stripmap ascending data.

II. Problem Formulation and General Description of the Proposed Method

A. General Hypothesis

Preliminary steps such as image coregistration and radiometric calibration of the SAR images are not developed in this paper. Nevertheless, these two steps are very important for every change detection method because they may affect the change detection result.

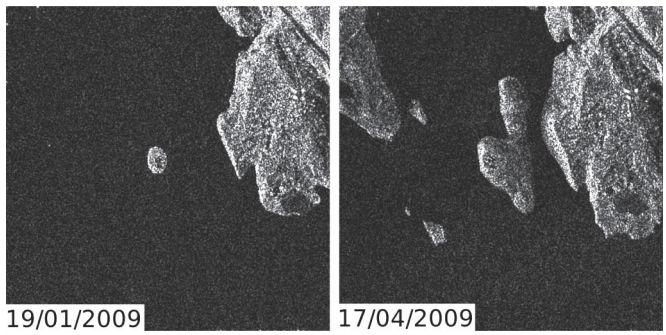

Fig. 1. Two coregistered TerraSAR-X Stripmap amplitude images acquired over the Serre–Ponçon Lake in south of France. The amplitude changes are due to water level differences between the two acquisitions.

We consider that the empirical amplitude distribution of each SAR image used for change detection is modeled by a Fisher probability density function (pdf) [25]. We can note that another statistical model could be used as well. We will consider that an amplitude value x in a SAR image is the resulting product of a texture t (the ideal denoised amplitude value), and speckle noise s

$$x = t \cdot s. \tag{1}$$

We consider that speckle noise s is modeled by a normalized Rayleigh–Nakagami distribution $\mathcal{RN}[1, L]$ and that texture t is modeled by an inverse Rayleigh–Nakagami distribution $\mathcal{RNI}[\mu, M]$. Thus, using the Mellin convolution $\hat{\star}$, the resulting Fisher distribution $\mathcal{F}_A[\mu, L, M]$ of the amplitude values x is expressed as [25]

$$\mathcal{F}_A[\mu, L, M] = \mathcal{RNI}[\mu, M] \,\hat{\star}\, \mathcal{RN}[1, L]. \tag{2}$$

The expressions of the latter distributions are detailed in Appendix A.

B. Generalized Temporal Means of SAR Amplitude Images

Temporal means are often used to deal with SAR image time series. For example, an average image can be computed from a time series in order to obtain a despeckled image. In most cases, a geometric, arithmetic, or quadratic mean is used. However, several generalized means are defined in the literature. Let us consider a set of N samples $T = \{x_1, \ldots, x_N\}$, the kth order Hölder mean [26] (or well-known "power mean") of these samples is defined as

$$\mathcal{M}_k[T] = \begin{cases} \sqrt[k]{\frac{1}{N}\sum_{i=1}^{N} x_i^k}, & \forall\, k \in \mathbb{R}^* \\ \sqrt[N]{\prod_{i=1}^{N} x_i}, & \text{if } k = 0. \end{cases} \tag{3}$$

Depending on the value of parameter k, the Hölder mean corresponds to particular means [26]. For example, the harmonic, geometric, arithmetic, and quadratic means respectively correspond to $k = -1, 0, 1,$ and 2.

In order to compare the different mean images obtained with different k values in the Hölder mean, we present in Fig. 1 two coregistered TerraSAR-X Stripmap amplitude images acquired over Serre–Ponçon Lake in the south of France. The amplitude

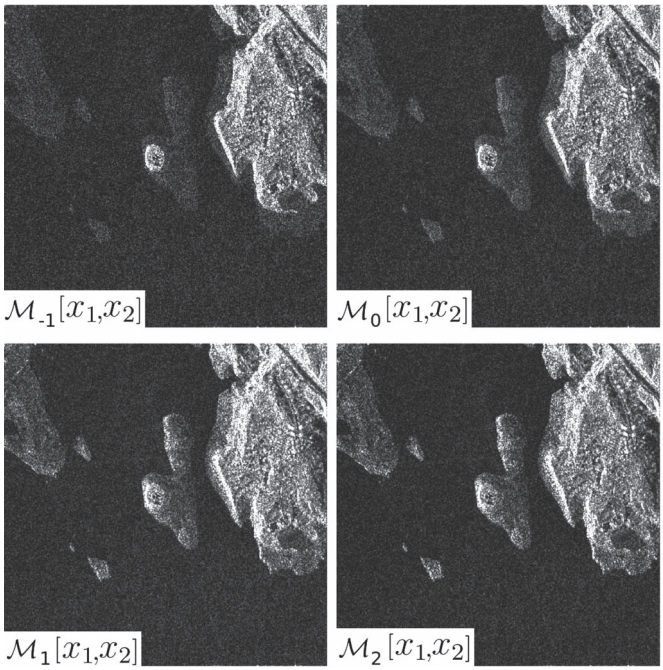

Fig. 2. Temporal means between the two amplitude images presented in Fig. 1, represented by x_1 and x_2. The differences between the four means are enhanced in the changed areas, whereas the four means are similar in the unchanged areas.

changes are due to water level differences between the two acquisition dates. As an example, four different temporal Hölder means between these two images are presented in Fig. 2, for $k = -1, 0, 1,$ and 2. Depending on parameter k, we observe that the resulting mean image can be very different over the changed areas. Over the unchanged areas, the four mean images are similar. The two particular TerraSAR-X images presented in Fig. 1 were chosen because they visually illustrate the different properties of the mean images depending on the k value.

On this particular example using only two SAR amplitude images, we observe an interesting behavior of the temporal means, which enables change detection along time series by comparing only two different temporal means. The MIMOSA method is based on this observation.

III. Automatic Change Detection Procedure for Image Pairs

A. MIMOSA Block Scheme for Image Pairs

In this section, we focus on change detection between two coregistered amplitude images x_1 and x_2. We consider that the two images share the same texture pattern t, which corresponds to the assumption that no change occurred between the two acquisitions. The two images x_1 and x_2 are only distinguished by their speckle noise values s_1 and s_2, respectively. Thus, the problem can be formulated under the following system:

$$\begin{cases} x_1, & t \cdot s_1 \\ x_2, & t \cdot s_2. \end{cases} \tag{4}$$

We assume that texture t is modeled by an inverse Rayleigh–Nakagami distribution $p_t(t) = \mathcal{RNI}[\mu, M](t)$. We also consider that the two speckle values s_1 and s_2 are different and modeled by the same normalized Rayleigh–Nakagami distribution $p_s(s) = \mathcal{RN}[1, L](s)$.

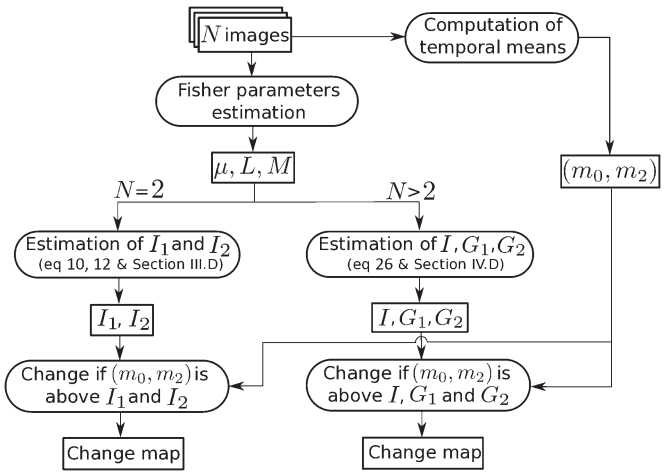

Fig. 3. Block scheme of the MIMOSA method in the case of change detection between image pairs ($N = 2$; see Section III-A) and along time series ($N > 2$; see Section IV-A). The geometric mean m_0 and quadratic mean m_2 are used.

The three steps of the MIMOSA method are presented in the following: 1) estimation of the amplitude distributions parameters; 2) estimation of the joint pdf between the two considered temporal means; and 3) automatic threshold selection.

In order to clarify the MIMOSA method and to enable a simple implementation by the reader, a general block scheme of the method is presented in Fig. 3. This block scheme refers not only to the present case of image pairs but also to the case of time series, which is described in Section IV.

B. Step 1: Estimation of the Amplitude Distributions Parameters

The aim of this step is to estimate the three statistical parameters (i.e., μ, L, and M) of the Fisher distribution in the amplitude images. Under the assumption that both images share the same texture t and that both speckle noise values are modeled by the same distribution, the three parameters μ, L, and M should be similar in both images. Thus, with real data where changed pixels are often marginal among the complete SAR images, the parameter estimation is performed over the union of the amplitude samples contained in both images, as if it were one single image. Indeed, the estimated parameters represent a tradeoff between the parameters that would have been estimated on the two images separately. This tradeoff can take into account the presence of changed areas. Parameter estimation is performed using a log-cumulant-based method [27], [28].

C. Step 2: Estimation of the Joint and Conditional PDF Between the Two Considered Temporal Means

Let consider two different Hölder means m_0 (the geometric mean) and m_k (with $k > 0$) between both images x_1 and x_2, which are expressed as

$$\begin{cases} m_0 = \mathcal{M}_0\left[\{x_1, x_2\}\right] = \sqrt{x_1 x_2} & = t \cdot \sqrt{s_1 s_2} \\ m_k = \mathcal{M}_k\left[\{x_1, x_2\}\right] = \sqrt[k]{\frac{x_1^k + x_2^k}{2}} & = t \cdot \sqrt[k]{\frac{s_1^k + s_2^k}{2}}. \end{cases} \tag{5}$$

The aim of this step is the estimation of the joint pdf $p_{m_0m_k}(m_0, m_k)$. This pdf predicts the points repartition in the empirical scatterplot between m_0 and m_k without changes between the images. Thus, the theoretical pdf is compared with the observed scatterplot in order to detect the changes. First, the computation of $p_{m_0m_k}(m_0, m_k)$ begins with the computation of $p_{12}(x_1, x_2)$. Then, as described in the following, $p_{12}(x_1, x_2)$ is transformed into $p_{m_0m_k}(m_0, m_k)$ through a variable change.

As t is assumed to be known, we define the conditional probabilities of the amplitude values x_1 and x_2 under the knowledge of t, according to the multiplicative model described in (4)

$$\begin{cases} p_1(x_1|t) = \frac{1}{t} p_s\left(\frac{x_1}{t}\right) \\ p_2(x_2|t) = \frac{1}{t} p_s\left(\frac{x_2}{t}\right). \end{cases} \tag{6}$$

The assumption that the texture t is known does not imply a real texture estimation over the images. Indeed, the texture pattern is only modeled by a statistical distribution and has not to be estimated. Since the two variables x_1 and x_2 are independent through the independence of their respective speckle values s_1 and s_2 once t has been fixed, the joint probability between x_1 and x_2 under the knowledge of t can be expressed as

$$p_{12}(x_1, x_2|t) = p_1(x_1|t)p_2(x_2|t) = \frac{1}{t^2} p_s\left(\frac{x_1}{t}\right) p_s\left(\frac{x_2}{t}\right). \tag{7}$$

By integration, we express the joint probability linking x_1 and x_2 without the need to know the value of t using the $p_t(t)$ distribution

$$p_{12}(x_1, x_2) = \int_0^{+\infty} p_s\left(\frac{x_1}{t}\right) p_s\left(\frac{x_2}{t}\right) p_t(t) \frac{dt}{t^2}. \tag{8}$$

Using the Fisher model, the joint pdf $p_{12}(x_1, x_2)$ can be expressed (see Appendix B) as

$$p_{12}(x_1, x_2) = \frac{4(x_1x_2L)^{2L}(\mu^2 M)^M A^{-(2L+M)}\Gamma(2L+M)}{\Gamma(L)^2\Gamma(M)x_1x_2} \tag{9}$$

where $A = L(x_1^2 + x_2^2) + M\mu^2$.

In Appendix C, we show that strictly equivalent expressions of $p_{12}(x_1, x_2)$ can be found in [17]–[19]. Indeed, in the case of a homogeneous texture, $p_{12}(x_1, x_2)$ is a BGD. Thus, (9) is a generalization of the BGD.

Fig. 4 shows the theoretical joint pdf $p_{12}(x_1, y_2)$ in the case of a Fisher distribution of parameters $\mu = 156.22$, $L = 1.02$, and $M = 4.44$, as compared to the observed scatterplot of the coregistered amplitude images where the Fisher parameters were estimated. The data used here are CARABAS images. We can note that in [20]–[22], the pdf between the two amplitude images is estimated from the observed scatterplot. In our case, the pdf is directly evaluated from the amplitude distribution parameters under the hypothesis that no change occurred.

In order to achieve step 2, the transformation from $p_{12}(x_1, x_2)$ to $p_{m_0m_k}(m_0, m_k)$ is finally performed through a variable change using the Jacobian J_k of the system presented

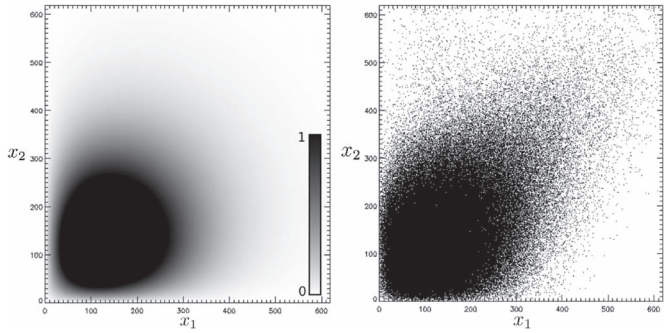

Fig. 4. (Left) Theoretical joint pdf $p_{12}(x_1, x_2)$ between two images following Fisher distributions of parameters $\mu = 156.22$, $L = 1.02$, and $M = 4.44$, sharing the same texture. The pdf data are normalized between 0 and 1. (Right) Associated observed scatterplot of the coregistered CARABAS amplitude images on which the Fisher parameters were estimated.

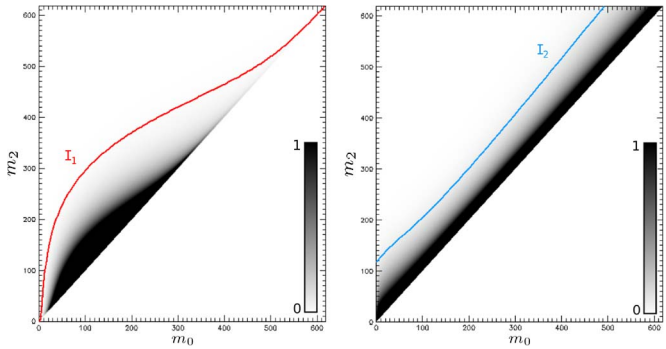

Fig. 5. (Left) Theoretical joint pdf $p_{m_0m_2}(m_0, m_2)$ for two images following Fisher distributions with parameters $\mu = 156.22$, $L = 1.02$, and $M = 4.44$, sharing the same texture. The red line represents isoline I_1 (see Section III-D). (Right) Conditional pdf $p_{m_2|m_0}(m_2|m_0)$. The blue line represents isoline I_2 (see Section III-D). The pdf data are normalized between 0 and 1.

in (5). Thus, we express the joint probability $p_{m_0m_k}(m_0, m_k)$ as a function of the solutions of the system x_1 and x_2

$$p_{m_0m_k}(m_0, m_k) = \frac{2 \cdot p_{12}(x_1, x_2)}{|J_k(x_1, x_2)|} \tag{10}$$

where the Jacobian operator is defined as

$$J_k(x_1, x_2) = \frac{\mathcal{M}_k[x_1, x_2]\left(x_2^k - x_1^k\right)}{2\mathcal{M}_0[x_1, x_2]\left(x_1^k + x_2^k\right)}. \tag{11}$$

Note that $p_{m_0m_k}(m_0, m_k)$ is limited to the part of the plane where m_0 and m_k are positive.

Fig. 5 shows on the left the theoretical joint pdf $p_{m_0m_k}(m_0, m_k)$ in the case of a Fisher distribution of parameters $\mu = 156.22$, $L = 1.02$, and $M = 4.44$ in the case of $k = 2$. Since the changes are located off the diagonal in the (x_1, x_2) scatterplot, the changes are also located off the diagonal in the (m_0, m_2) scatterplot. Near the diagonal, the points correspond to no change. The particular m_0 (geometric) and $m_k = m_2$ (quadratic) means are chosen to be consistent with the case of time series (see Section IV), where the choice of these two means m_0 and m_2 is motivated by computational constraints. In the two-image case, other Hölder means could have been chosen.

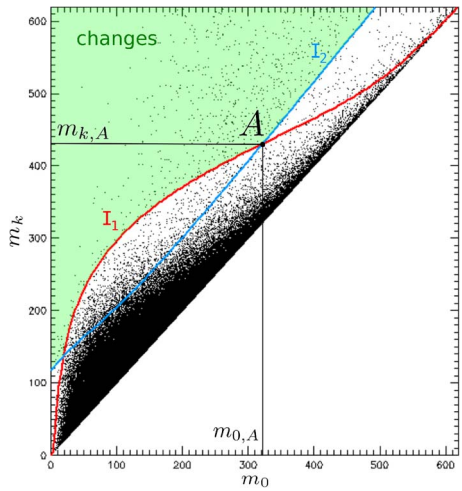

Fig. 6. Observed scatterplot $(m_0, m_{k=2})$ for two coregistered amplitude images following Fisher distributions with estimated parameters $\mu = 156.22$, $L = 1.02$, and $M = 4.44$. The red line represents the isoline of probability I_1, associated to the joint pdf, whereas the blue line represents the isoline I_2 associated to the conditional pdf (see Section III-D). The changed pixels correspond to the points above both isolines I_1 and I_2. The second intersection point A between I_1 and I_2 is defined as $(m_{0,A}|m_{k,A})$. The area of the scatterplot detected as changes is indicated in green.

The $p_{m_0m_k}(m_0, m_k)$ joint pdf predicts the most likely locations for the points in the associated scatterplot, which is presented in Fig. 6. However, we note that the high valued outliers exhibit a very low probability according to $p_{m_0m_k}(m_0, m_k)$ even if they are close from the diagonal of the scatterplot and thus correspond to a no-change case (see points with $m_0 > 400$ on Fig. 6). This problem is due to the texture model, i.e., the $\mathcal{RNI}$ distribution, which predicts that the high valued samples are rare. These high valued outliers, which are close to the diagonal, generally correspond to stable scatterers that strongly reflect the radar signal and that should not be selected as changes. Thus, thresholding the joint pdf only is not sufficient to detect changes because the high valued pairs of means would be detected as changes even if they are almost equal. We can mention that the same problem occurs for low valued outliers. Moreover, this problem would also occur with other classical distribution models for the texture, such as $\mathcal{RN}$ instead of the $\mathcal{RNI}$ distribution.

To overcome this problem, the conditional probability is used in complement of the joint probability. The conditional distribution of m_k under the knowledge of m_0, defined as $p_{m_k|m_0}(m_k|m_0)$, can be computed using the joint pdf $p_{m_0m_k}(m_0, m_k)$

$$p_{m_k|m_0}(m_k|m_0) = \frac{p_{m_0m_k}(m_0, m_k)}{\int_{m_0}^{+\infty} p_{m_0m_k}(m_0, z)\, dz}. \qquad (12)$$

No simple explicit expression could be obtained for $p_{m_k|m_0}(m_k|m_0)$. Nevertheless, the integral in (12) can be easily evaluated numerically using standard numerical integration techniques.

Fig. 5 shows on the right the conditional pdf $p_{m_k|m_0}(m_k|m_0)$ in the case of a Fisher distribution of parameters $\mu = 156.22$, $L = 1.02$, and $M = 4.44$ in the case of $k = 2$.

The conditional pdf $p_{m_k|m_0}(m_k|m_0)$ predicts that the two means m_0 and m_k are more likely to be close to each other, whatever their values. Thus, $p_{m_k|m_0}(m_k|m_0)$ is also thresholded in addition of $p_{m_0m_k}(m_0, m_k)$ in order to prevent the pairs of means located near the diagonal of the scatterplot to be detected as changes. Indeed, the pairs of amplitude values corresponding to no change $(\mathcal{H}_0)$ can be distinguished according to the two following cases in the (m_0, m_k) scatterplot:

1) points corresponding to a high probability of apparition, which are defined by high values of $p_{m_0m_k}(m_0, m_k)$ or;
2) points that are located near the diagonal of the diagram, whatever their value. These points are defined by high values of $p_{m_k|m_0}(m_k|m_0)$.

Thus, considering the latter definition, we can define the change case $\mathcal{H}_1$ and the no-change case $\mathcal{H}_0$ as

$$\begin{aligned} \mathcal{H}_0 &: p_{m_0m_k}(m_0, m_k) \geq \lambda_1 \vee p_{m_k|m_0}(m_k|m_0) \geq \lambda_2 \\ \mathcal{H}_1 &: p_{m_0m_k}(m_0, m_k) < \lambda_1 \wedge p_{m_k|m_0}(m_k|m_0) < \lambda_2 \end{aligned} \qquad (13)$$

where λ_1 and λ_2 are the two different thresholds used to detect the changes. The automatic estimation of λ_1 and λ_2 for a given false alarm rate (FAR) is described in the next section.

The detection threshold λ_1 defines an isoline of probability I_1 in the $p_{m_0m_k}(m_0, m_k)$ pdf (see the left side of Fig. 5), whereas the detection threshold λ_2 defines an isoline I_2 in the $p_{m_k|m_0}(m_k|m_0)$ distribution (see the right side of Fig. 5).

In the MIMOSA method, both thresholds λ_1 and λ_2 are necessary because they are complementary. Indeed, when λ_1 value increases, thresholding only the joint pdf would detect as changes the high valued and low valued samples, only because they are rare according to the texture model (I_1 gets very close to the diagonal for low and high valued samples). Moreover, when λ_2 value increases, I_2 gets closer to the diagonal and can cross the dense part of the scatterplot, generating a lot of false alarms among medium values if only $p_{m_k|m_0}(m_k|m_0)$ was thresholded.

As an example, in the GLRT [13] change detection technique, the ratio between arithmetic mean m_1 and geometric mean m_0 is compared to a simple threshold. Thus, the GLRT detects changes for pairs of means (m_0, m_1) located over an affine line in the (m_0, m_1) scatterplot. This affine selection generates a very high number of false alarms, particularly in the low and medium values, since the corresponding dense part of the scatterplot can be crossed by the affine line. Unlike the GLRT technique, the MIMOSA method takes into account the most likely locations of points in the scatterplot using I_1 to keep the dense part of the scatterplot in the no-change area.

D. Step 3: Automatic Threshold Selection

This part describes the automatic estimation of the change detection thresholds λ_1 and λ_2, estimated from a given FAR, which is the only parameter of the MIMOSA method. Threshold λ_1 is estimated first; λ_2 depends on λ_1.

Detecting changes by thresholding $p_{m_0m_k}(m_0, m_k)$ corresponds to select the points in the scatterplot plane, which are located above this isoline I_1. Let D be the part of the (m_0, m_k) plane located above the isoline I_1, where m_0 and m_k are

positive. Because $p_{m_0m_k}(m_0, m_k)$ has been estimated under the hypothesis $\mathcal{H}_0$ that no change occurred between the two acquisitions, FAR P_{fa} is defined as

$$P_{\text{fa}} = \iint\limits_{(m_0,m_k)\in D} p(m_0, m_k)\, d\, m_0\, d\, m_k. \tag{14}$$

Thus, for a given FAR P_{fa}, we precisely evaluate the corresponding threshold value λ_1 using an iterative technique. In practice, the joint pdf $p_{m_0m_k}(m_0, m_k)$ is computed over a 1000×1000 square window in the (m_0, m_k) space and is normalized. The boundaries of the estimation are fixed by the image statistics. Indeed, the estimation of the joint pdf $p_{m_0m_k}(m_0, m_k)$ is limited to the part of the space where m_0 and m_k are lower than 10μ, where μ is the parameter of the Fisher distribution corresponding to the data. Once the pdf has been computed, a dichotomy is used to precisely estimate the threshold value λ_1.

Once λ_1 has been estimated, the second threshold λ_2 can be estimated. We recall that thresholding only the joint pdf $p_{m_0m_k}(m_0, m_k)$ using λ_1 is not sufficient to detect changes because the high valued pairs of means would be detected as changes even if almost equal. In order to estimate λ_2, the tail of the texture distribution is first isolated using the cumulative distribution of the inverse Rayleigh–Nakagami distribution, defined as

$$R[\mu, M](y) = \int_0^y \mathcal{RNI}[\mu, M](z)\, dz. \tag{15}$$

The size of the tail of the texture distribution depends on parameter M. Indeed, when M is large ($\gg 1$), the texture distribution is centered around the μ value and does not have a heavy tail, which corresponds to very homogeneous texture data. On the contrary, when M is small (< 1), the texture distribution presents a heavy tail that corresponds to very heterogeneous texture values, with many high valued outliers. Thus, the part of the distribution tail to be selected depends on the value of M. The lower M is, the larger is the percentage β of the tail to select. We propose an empirical formulation of the percentage β using the cumulative distribution of the texture distribution R, which is expressed as

$$\beta = p_{\min} + (p_{\max} - p_{\min}) \exp\left(-\frac{M}{M_c}\right) \tag{16}$$

where $\beta \in [p_{\min}, p_{\max}]$; M is the Fisher distribution parameter estimated over the data; the two parameters $p_{\max}$ and $p_{\min}$ are the maximum and minimum parts, respectively, of the distribution to consider as the tail; and M_c is the critical value of M corresponding to the change of texture behavior between heterogeneous and homogeneous data samples. We will see in Section V-A that good results are obtained when $p_{\max}$ is set to 10% (0.1), whereas $p_{\min}$ is set to 1% (0.01), and M_c is set to 1. These particular values are well adapted for various data configurations. These values were experimentally validated as they produced good results with different sensors, wavelengths, and acquisition modes. Using an iterative technique, we precisely evaluate the texture value $m_{0,A}$ corresponding to the lower tail limit, implicitly defined through the following relation:

$$R[\mu, M](m_{0,A}) = 1 - \beta. \tag{17}$$

In practice, $m_{0,A}$ is estimated using a dichotomy over the cumulative distribution R. High valued pairs of means that are close from the diagonal are detected as changes by thresholding only $p_{m_0m_k}(m_0, m_k)$ because the isoline I_1 is too close from the diagonal for high mean values. Thus, when $m_0 > m_{0,A}$, thresholding of $p_{m_k|m_0}(m_k|m_0)$ using λ_2 is preferred. We define the intersection point $A = (m_{0,A}, m_{k,A})$ between two isolines I_1 and I_2, such as $p_{m_0m_k}(m_{0,A}, m_{k,A}) = \lambda_1$. The value of $m_{k,A}$ is then precisely evaluated using a simple iterative technique over $p_{m_0m_k}(m_0, m_k)$. Finally, the explicit value of the second change detection threshold λ_2 can be obtained as

$$\lambda_2 = p_{m_k|m_0}(m_{k,A}|m_{0,A}). \tag{18}$$

The global change detection procedure finally consists in a double thresholding of $p_{m_0m_k}(m_0, m_k)$ using λ_1 and $p_{m_k|m_0}(m_k|m_0)$ using λ_2 according to the relation exposed in (13). Thus, the final detected changes are the points in the scatterplot, which are located above the two isolines I_1 and I_2 (see Figs. 3 and 6).

IV. Automatic Change Detection Procedure for Time Series

A. MIMOSA Block Scheme for Time Series

In this part, we consider a time series of N images, defined as $T = \{x_1, x_2, \ldots, x_N\}$. Under the hypothesis that no change occurred during this time series, we consider that all the amplitude images x_i share the same texture t. Thus, each amplitude value x_i is distinguished by a speckle noise s_i and can be defined as

$$\forall\, i \in [1, N],\ x_i = t \cdot s_i. \tag{19}$$

The same distribution model as in the two-image case (see Section III-A) is used for the texture and speckle distributions. Indeed, we consider again that the texture t is modeled by an inverse Rayleigh–Nakagami distribution $p_t(t) = \mathcal{RNI}[\mu, M](t)$ and that the different speckle values s_i are modeled by the same normalized Rayleigh–Nakagami distribution $p_s(s) = \mathcal{RN}[1, L](s)$. The three steps of the MIMOSA method applied to time series are presented in Fig. 3 in Section III-A. They are described in the following.

B. Step 1: Estimation of the Amplitude Distributions Parameters

The estimation of the three Fisher distribution parameters μ, L, and M is performed using the same log-cumulant-based method as in the two-image case. Parameter estimation is performed over the union of the amplitude samples contained in the time series, as if it were one single image.

C. Step 2: Estimation of the Joint PDF Between m_0 and m_2

In this section, we propose a very simple choice based only on two means m_0 and m_2. In order to estimate the joint pdf between m_0 and m_2, related to the (m_0, m_2) scatterplot, the problem can be then formulated as

$$\begin{cases} m_0 = \sqrt[N]{\prod_{i=1}^{N} t \cdot s_i} = t \cdot \mathcal{M}_0\left[\{s_i\}\right] \\ m_2 = \sqrt{\frac{1}{N}\sum_{i=1}^{N} t^2 \cdot s_i^2} = t \cdot \mathcal{M}_2\left[\{s_i\}\right]. \end{cases} \tag{20}$$

Let it be emphasized that the latter system is a generalization of (4). The problem consists in a two-equation system with N variables. Thus, because the number of images in the time series is assumed to be greater than two, this system cannot be solved without any assumption. Therefore, in order to deal with the N unknown speckle values s_i, only their average values along the time series are considered. Let $p_{\mathcal{M}_0}$ and $p_{\mathcal{M}_2}$ be defined as the distributions respectively followed by the geometric and quadratic means of the N variables s_i. Thus, the conditional probabilities of m_0 and m_2 under the knowledge of t can be expressed as

$$\begin{cases} p(m_0|t) = \frac{1}{t} p_{\mathcal{M}_0}\left(\frac{m_0}{t}\right) \\ p(m_2|t) = \frac{1}{t} p_{\mathcal{M}_2}\left(\frac{m_2}{t}\right). \end{cases} \tag{21}$$

Let us define an estimator $\hat{p}(m_0, m_2|t)$ of the conditional joint pdf between the two means m_0 and m_2 under the knowledge of t. Following the same framework as in the two-image case, we make the hypothesis that this estimator is defined as

$$\hat{p}(m_0, m_2|t) \triangleq p(m_0|t)\, p(m_2|t). \tag{22}$$

By integration, we can express the joint pdf linking m_0 and m_2, without the need to know the value of t using the $p_t(t)$ distribution

$$\hat{p}(m_0, m_2) \triangleq \int_0^{+\infty} p_{\mathcal{M}_0}\left(\frac{m_0}{t}\right) p_{\mathcal{M}_2}\left(\frac{m_2}{t}\right) p_t(t) \frac{dt}{t^2}. \tag{23}$$

We can remark that no Jacobian operator is used to express the latter joint pdf, unlike the two-image case [see (10)]. Indeed, the rigorous use of a Jacobian operator would have involved the definition of N different means to create N equations instead of two in (20). Then, the pdf linking these N different means should have been evaluated and integrated $(N-2)$ times in order to compute the $p(m_0, m_2)$ pdf. This evaluation is of course unrealistic. Thus, the definition of the $\hat{p}(m_0, m_2)$ estimator is necessary. Because of the hypothesis in (22), $\hat{p}(m_0, m_2)$ is defined and strictly positive for $m_2 < m_0$, which is impossible because the order relation $m_0 \leq m_2$ [26]. Thus, $\hat{p}(m_0, m_2)$ is biased. This bias is due to the representation of the mean speckle values through the independent distributions $p_{\mathcal{M}_0}$ and $p_{\mathcal{M}_2}$, where the two expressions are not linked to satisfy the order relation $m_0 \leq m_2$. Moreover, $\hat{p}(m_0, m_2)$ in the $N = 2$ case is not equivalent to (10). To cope with the condition $m_0 \leq m_2$ [26], we define $\hat{p}(m_0, m_2) = 0$ if $m_2 < m_0$. Despite the fact that the estimator $\hat{p}(m_0, m_2)$ is biased, we show that the evaluated pdf fits very well the associated observed scatterplot, as long as $\hat{p}(m_0, m_2)$ is set to zero if $m_0 < m_2$ (see Fig. 7).

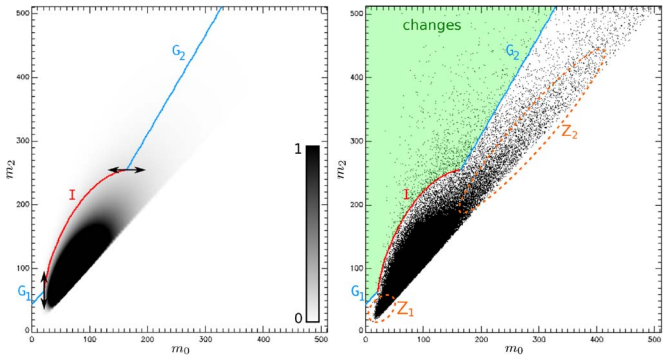

Fig. 7. (Left) Joint pdf $\hat{p}(m_0, m_2)$ for $N = 7$ images following Fisher distributions. The pdf data are normalized between 0 and 1. (Right) Associated observed scatterplot. The $\hat{p}(m_0, m_2)$ isoline I is represented in red. Two additional guides G_1 and G_2, which are used to prevent the detection of points near the diagonal, are represented in blue. The horizontal and vertical tangents of the I isoline are indicated with the two black double arrows on the pdf. The area of the scatterplot detected as changes is indicated in green. The two circled areas Z_1 and Z_2 respectively correspond to low valued and high valued stable pixels.

In order to express the joint pdf between m_0 and m_2 under the Fisher distribution model, $p_{\mathcal{M}_2}$ and $p_{\mathcal{M}_0}$ must be calculated. The choice of these two particular means is based on computational constraints related to the calculation of $p_{\mathcal{M}_2}$ and $p_{\mathcal{M}_0}$, which are the simplest cases to compute. Indeed, the calculation of $p_{\mathcal{M}_2}$ is carried out due to particular properties of the Gamma distribution $\mathcal{G}$, whereas the calculation of $p_{\mathcal{M}_0}$ is carried out using the Meijer G-functions $\overline{G}$ defined in [29] (see Appendix E).

First, the distribution followed by the quadratic mean of N samples following a normalized Rayleigh–Nakagami distribution $\mathcal{RN}[1, L]$ is expressed as follows (see Appendix D):

$$p_{\mathcal{M}_2}(z) = 2z\mathcal{G}[1, NL](z^2). \tag{24}$$

Then, the distribution followed by the geometric mean of N samples following a normalized Rayleigh–Nakagami distribution $\mathcal{RN}[1, L]$ is expressed as follows [37] [see (49) in Appendix E]:

$$p_{\mathcal{M}_0}(z) = \frac{2N}{z\Gamma(L)^N} \overline{G}_{0,N}^{N,0}\left(z^{2N} L^N \,\middle|\, \begin{matrix} \cdot \\ \underbrace{L, \ldots, L}_{N} \end{matrix} \; ; \; \begin{matrix} \cdot \\ \cdot \end{matrix}\right). \tag{25}$$

Finally, $p_{\mathcal{M}_2}$ and $p_{\mathcal{M}_0}$ are used to obtain $\hat{p}(m_0, m_2)$, which is expressed in (26), shown at the bottom of the next page as a Meijer function [see (50) in Appendix E]. The Meijer function corresponding to $\hat{p}(m_0, m_2)$ is precisely evaluated numerically. Indeed, the implementation of the Meijer functions is easier in the present case because only two lists of parameters among the four possible are used (see Appendix E). Note that $\hat{p}(m_0, m_2)$ does not correspond to (10) if $N = 2$. This is due to the fact that $\hat{p}(m_0, m_2)$ is only an estimator.

We present in Fig. 7 the theoretical joint pdf $\hat{p}(m_0, m_2)$ for $N = 7$ images, as compared with the observed scatterplot.

The distribution of the points in the scatterplot is well predicted by the evaluated pdf. We define I as the isoline in the pdf defined by relation $\hat{p}(m_0, m_2) = \lambda$, where λ is the change detection threshold. Thresholding only $\hat{p}(m_0, m_2)$ would once again detect as changes all the points located near the diagonal of the scatterplot. Thus, an additional guide must be applied to the scatterplot to prevent the points located near the diagonal to be selected as changes. This automatic threshold estimation and the definition of the complementary guide are described in the next section.

D. Step 3: Automatic Threshold Selection

The automatic estimation of the change detection threshold follows the same procedure as in the two-image case. From a given FAR P_{fa}, the threshold value λ is automatically estimated using standard iterative techniques, according to the following relation:

$$P_{\text{fa}} = \iint\limits_{(m_0,m_2)\in D'} \hat{p}(m_0, m_2)\, d\, m_0\, d\, m_2 \tag{27}$$

where D' is defined as the area of the (m_0, m_2) plane located over the isoline I, where m_0 and m_2 are positive. It is analog to the D area that was defined for image pairs [see (14)].

If the changes are detected using only the thresholding of the joint pdf $\hat{p}(m_0, m_2)$, points located near the diagonal in the scatterplot would be detected as changes for very high or very low values. Thus, additional guides must be applied to the scatterplot. Considering the expression of the joint pdf $\hat{p}(m_0, m_2)$, it is not possible to obtain the conditional pdf $\hat{p}(m_2|m_0)$. Thus, simple guides must be defined without using the conditional pdf, unlike the two-image case.

Because the $\hat{p}(m_0, m_2)$ estimator is biased, the threshold value λ defines an isoline I in the pdf, which can form a loop that crosses the diagonal of the diagram. However, only the top part of the isoline is useful. Thus, in order to overcome the limits of the model, we propose to define the additional guides G_1 and G_2 from the shape of the isoline I:

1) G_1: defined until the point where I becomes vertical;
2) G_2: defined from the point where I becomes horizontal.

G_1 is dedicated to low valued points near the diagonal (see dashed ellipse Z_1 on the right side of Fig. 7), which represent the low valued stable points along the time series. Thus, because the points corresponding to no change are located near the diagonal, whatever their value, we propose to define G_1 as a line parallel to the diagonal. In addition, we can mention that G_1 prevents the points affected by quantification effects to be detected as changes. The second guide, i.e., G_2, is dedicated to high valued points near the diagonal (see dashed ellipse Z_2 on the right side of Fig. 7), which represent the high valued stable points along the time series. We propose to define G_2 as an affine line crossing the point where I becomes horizontal and the origin, as indicated on the right of Fig. 7. Guide G_2 is inspired by the GLRT technique.

G_1 and G_2 are necessary in addition of I because the presence of points in the areas Z_1 and Z_2 is not predicted by the joint pdf $\hat{p}(m_0, m_2)$ alone. Indeed, as the dependence between m_0 and m_2 is not taken into account, high or low valued pixels along the whole time series are very improbable (see dashed ellipses Z_1 and Z_2 on the right side of Fig. 7).

The global change detection procedure finally consists into a segmentation of the scatterplot according to the successive usage of G_1, I, and G_2 depending on the m_0 value (see Fig. 3). Only the pairs of means located over the union of these three limits are detected as changes so that the pairs of means corresponding to the most likely positions in the scatterplot are not detected as changes.

The method is not sensitive to the date of the changes within the time series since the images are merged in the two temporal means m_0 and m_2 without considering their respective dates. Moreover, a change due to a single image cannot be directly distinguished from a change involving several images.

$$\hat{p}(m_0, m_2) \propto m_2^{2NL-1} m_0^N \left(NLm_2^2 + M\mu^2\right)^{-\frac{N+1}{2}-NL-M} \overline{G}_{N,N}^{N,N}\left(\left(\frac{NLm_0^2}{NLm_2^2 + M\mu^2}\right)^N \middle| \begin{matrix} \{U_N\} \\ \underbrace{L-\frac{N+1}{2N}, \ldots, L-\frac{N+1}{2N}}_{N} \end{matrix} \begin{matrix} ; & \cdot \\ ; & \cdot \end{matrix}\right) \tag{26}$$

where :

$$\{U_N\} = \left\{ \underbrace{\ldots, \frac{-5}{2N}, \frac{-3}{2N}, \frac{-1}{2N}}_{\frac{N}{2}}, \underbrace{\frac{1}{2N}, \frac{3}{2N}, \frac{5}{2N}, \ldots}_{\frac{N}{2}} \right\} \quad \text{if } N \text{is even}$$

$$\{U_N\} = \left\{ \underbrace{\ldots, \frac{-6}{2N}, \frac{-4}{2N}, \frac{-2}{2N}}_{\frac{N-1}{2}}, 0, \underbrace{\frac{2}{2N}, \frac{4}{2N}, \frac{6}{2N}, \ldots}_{\frac{N-1}{2}} \right\} \quad \text{if } N \text{ is odd}$$

E. Taking Into Account an Incoming Image in the Time Series

As aforementioned, the data volume to process in order to detect the changes using the MIMOSA method is limited to the two temporal means m_0 and m_2, whatever the length of the time series. In this section, we describe how to update these two means using only a new incoming image x_{N+1} in the time series. Using this new amplitude image, the new means $m_{0,N+1}$ and $m_{2,N+1}$ of the $N+1$ images are estimated from the previous means $m_{0,N}$ and $m_{2,N}$ of the first N images according to the following two equations:

$$m_{0,N+1} = \sqrt[N+1]{m_{0,N}^{N} x_{N+1}} \tag{28}$$

$$m_{2,N+1} = \sqrt{\frac{N m_{2,N}^2 + x_{N+1}^2}{N+1}}. \tag{29}$$

Thus, the N previous images are not used to compute the two new means $m_{0,N+1}$ and $m_{2,N+1}$. Therefore, an operational process can be designed to deal with new incoming images in a time series, without processing the entire time series again, which is a great time-saver.

The parameters μ, L, and M that were used with the previous set of N images can be first used to detect changes on the $N+1$ images because the last incoming image is supposed to be similar to the others. Nevertheless, the three parameters may be later updated in order to refine the change detection on the new time series of $N+1$ images.

V. Results and Discussion

A. Change Detection Between Image Pairs

In this section, we present change detection results between two SAR amplitude images obtained with the MIMOSA method. We use the data from the VHF–Challenge set. The original data set contains 24 CARABAS-II magnitude images acquired during a flight campaign in Vidsel (Sweden) in 2002. During this campaign, a set of vehicles was used as concealed targets and moved between the different acquisitions dates.

We present in Fig. 8 the three types of vehicles used for the experiment. They present different sizes and characteristics. The particular deployment of 25 vehicles studied in this section is presented in Fig. 8, and it is considered as the ground truth.

The two particular images considered in this test are v02_2_1_1 and v02_4_1_1, as referenced in the original challenge paper. We have processed all the data provided in the 24-image set; this particular couple is shown as an illustration. The two amplitude images (zoomed over the test site) are presented in Fig. 8. The left image v02_2_1_1 exhibits the test area without the vehicle deployment, whereas the 25 vehicles are visible in the right image v02_4_1_1. The original data provided in the change detection challenge were processed by the MIMOSA method. No spatial filtering has been applied on the provided images. Moreover, no radiometric calibration or additional image coregistration has been performed.

The parameters of the amplitude distributions under the Fisher model estimated over the union of the amplitude samples contained in the two images are $\mu = 156.22$, $L = 1.02$, and

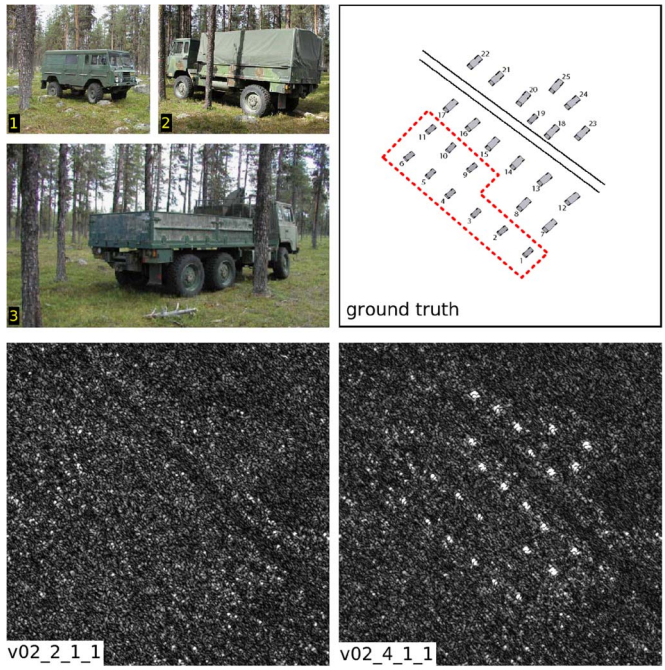

Fig. 8. (Upper left) Three types of vehicles used as concealed targets. (Upper right) Ground truth of the considered vehicle deployment, where a group of type-1 vehicles is circled in red. (Down) Zoom-in CARABAS-II amplitude images of the test site, where the vehicle deployment is visible in the right image v02_4_1_1 and can be compared with the ground truth.

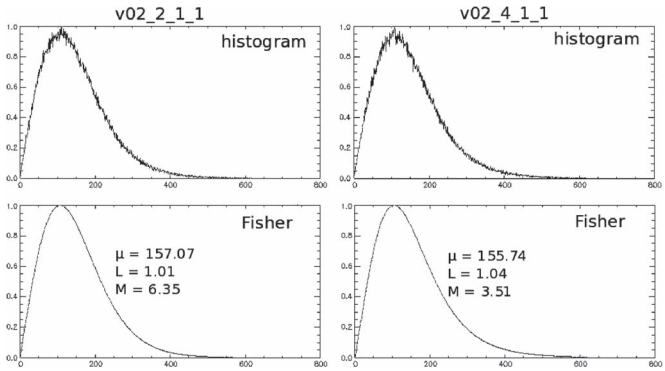

Fig. 9. (Up) Normalized histograms of the two amplitude images presented in Fig. 8. (Down) Normalized Fisher distributions estimated over the two amplitude images. The parameters $[\mu, L, M]$ of the Fisher distributions are presented on each curve.

$M = 4.44$. The respective histograms and associated Fisher distributions of the two images are presented in Fig. 9. We observe that the Fisher distributions fit very well the observed histograms. We can also note that the parameters of the two Fisher distributions estimated separately on the two images are close from the parameters estimated over the union of the amplitude samples. Moreover, the parameters estimated over the union of the images are a good tradeoff between the parameters estimated over the two images separately.

In this case, the geometric and quadratic means are used to detect the changes. The scatterplot and the associated joint pdf were already presented in Fig. 6 in Section III. The *a priori* FAR is fixed to 0.2%. The particular values to compute β [see (16)] are $p_{\max} = 0.1$, whereas $p_{\min} = 0.01$, and $M_c = 1$. Thus, $\beta \approx 0.011(1.1\%)$. The change detection results are presented

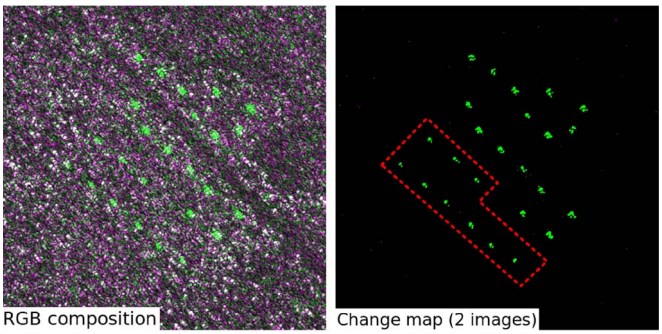

Fig. 10. (Left) RGB composition between the two amplitude images presented in Fig. 8. (Right) Automatic change detection result obtained with MIMOSA with an *a priori* FAR of 0.2%. Appearing bright items are represented in green; disappearing items are represented in magenta (not visible on the change map because they are very rare). A type-1 vehicle group is circled in red, illustrating that the vehicle size and orientation can be evaluated. No filtering operation has been applied to the change map.

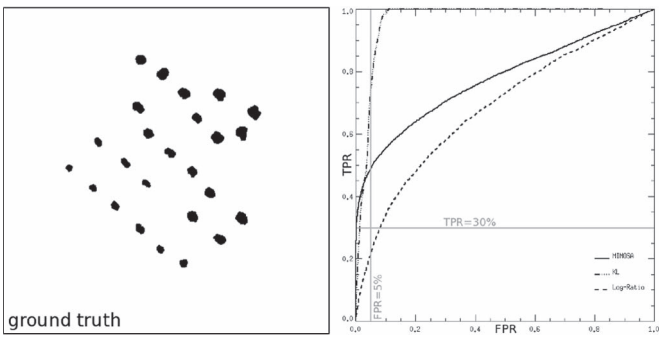

Fig. 11. (Left) Ground truth (reference change map) where the changes are represented in black. (Right) Experimental ROC curves for the log–ratio thresholding, Similarity measure using KL divergence and the MIMOSA method. Two isolines TPR $= 30\%$ and FPR $= 5\%$ are represented in gray.

on the right of Fig. 10. The change map has not been filtered. The map clearly shows that all 25 vehicles are well detected as appearing changes. We can also note that the different sizes of the different vehicles (see Fig. 8) are well visible and respected. The orientation of the detected changes, associated to the orientation of the vehicles, is also well conserved in the change map.

The results obtained with the MIMOSA method outperform the results obtained with other methods[30]–[36] using the same CARABAS-II public data. Unlike most results, all the targets are systematically detected with the MIMOSA method, whereas the shapes and sizes of the targets are also well respected. In [30], [31], [33], and [36] morphological operations are applied to the binary change maps to reduce the number of false alarms, unlike with our method where the number of false alarms is already very low without any postprocessing step. In [34] the change detection is limited to the computation of the ratio image, and no binary change map is provided. In [32] and [35] some vehicles are missed during the change detection, whereas the shapes of the vehicles are not well respected in [32], [35], and [36].

In order to provide numerical results, we compare the MIMOSA method to the log–ratio thresholding and to the similarity measure presented in [16]. The similarity measure is applied using a constant window size of 35 pixels $\times$ 35 pixels, which is the simple constant sized detector proposed in [16]. As a common reference for the three methods, we present on the left of Fig. 11, the change map, which is considered as ground truth. This map was generated according to the ground truth data provided in the CARABAS challenge, as presented on the upper right of Fig. 8 and with the colored RGB composition presented on the left of Fig. 10. A reasonable margin was respected around the changed pixels.

As well as for the MIMOSA method, the log–ratio thresholding and similarity measure are performed over the original data, without any spatial filtering. We present on the right of Fig. 11 the receiver operating characteristic (ROC) curve of the MIMOSA method compared with the two other methods. The ROC curves were computed according to the following equations:

$$\begin{cases} \text{TPR} = \dfrac{\text{TP}}{\text{TP+FN}} \\ \text{FPR} = \dfrac{\text{FP}}{\text{FP+TN}} \end{cases} \tag{30}$$

where TPR and FPR are respectively the true positive rate and false positive rate, whereas TP, FN, FP, and TN are respectively the numbers of true positive, false negative, false positive, and true negative detected pixels according to the ground truth. The FPR is also called FAR. Let us emphasize the fact that the different rates are estimated at the pixel level and not at the object level.

Since the values of TPR and FPR are strongly related to the shape of the ground truth image, whatever the method used, the ROC curves presented in Fig. 11 are only relevant if they are compared with each other. We observe that the ROC curve obtained with the MIMOSA method is always above the ROC curve obtained with the log–ratio thresholding, which shows that MIMOSA performs better than log–ratio. We observe that the MIMOSA ROC curve is also above the similarity measure ROC curve for low FARs ($< 3\%$). For higher FARs, the similarity measure ROC curve outperforms the two others.

Nevertheless, despite the fact that the similarity measure ROC curve is above the MIMOSA ROC curve, the change maps obtained with MIMOSA are visually more satisfying. Indeed, because it uses spatial neighborhoods, the similarity measure belongs to a different family than the MIMOSA method and the log–ratio thresholding, which are said to be pixel-by-pixel techniques. Thus, the different change maps must be carefully compared in addition to the ROC curves. As an example, we show in Fig. 12 the comparison of the change maps obtained with the three methods for the same TPR $= 30\%$ and for the same FPR $= 5\%$, which correspond to the two isolines represented on the ROC curves in Fig. 11. The particular TPRs of each vehicle are also indicated in Fig. 12 in order to show that some targets can be missed using the similarity measure despite the fact that the ROC curve predicts a very good global detection.

For the same global FPR $= 5\%$, the changes are well detected with the MIMOSA method, whereas they are barely visible among the false detections using the log–ratio thresholding. We also observe that some of the vehicles are totally missed using the similarity measure despite the fact that the similarity measure ROC curve is above the MIMOSA ROC curve for FPR $= 5\%$. Indeed, unlike the MIMOSA method,

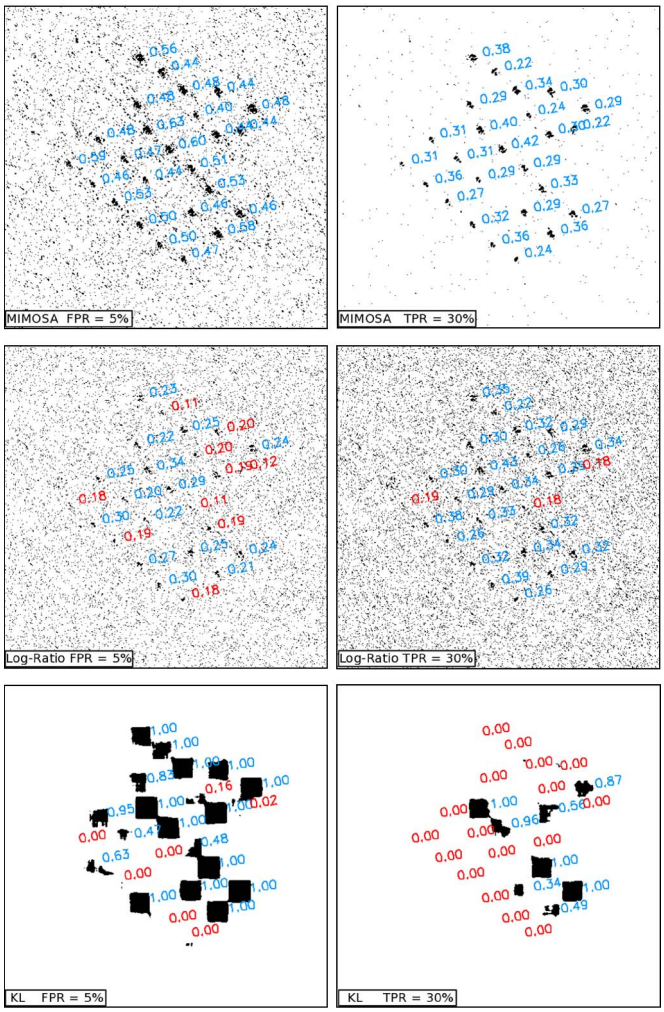

Fig. 12. Binary change maps obtained with (from top to bottom) the MIMOSA method, log–ratio thresholding, and similarity measure using KL divergence for (left) identical FPRs set to 5% and (right) TPRs set to 30%. The changes are represented in black. The TPR of each vehicle is respectively indicated in blue or red if it is higher or lower than 0.2 (20%).

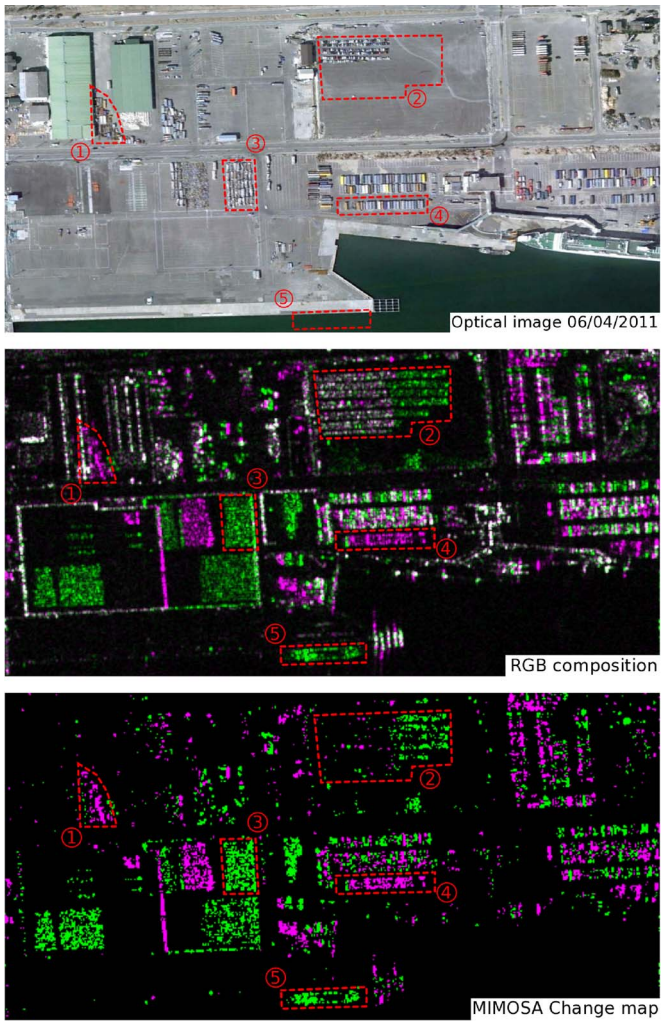

Fig. 13. From top to bottom: Optical image (Google Earth) of a container area in Sendai Harbor (06/04/2011), RGB composition between two coregistered TerraSAR-X amplitude images (06/05/2011–08/06/2011), and corresponding change map obtained with MIMOSA (*a priori* FAR set to 1%). The circled areas correspond to containers (1, 3, and 4), cars (2), and a boat (5).

the similarity measure does not use the full resolution and thus does not respect the shape of the changed areas. Indeed, we can observe that the change map exhibits squares that correspond to the shape of the window that is used. As a consequence, some changed areas corresponding to the vehicles can be totally covered and filled by these squares, corresponding to a particular TPR of 1. Thus, the global TPR increases even if some vehicles are not detected at all (particular TPR of these missed vehicles $= 0$). In this case, 10 vehicles among 25 are missed using the log–ratio thresholding, whereas 7 are missed using the similarity measure.

For the same global TPR $= 30\%$, we observe a very high number of false detections in the log–ratio map, whereas the MIMOSA map clearly exhibits the changed pixels with a very low number of false detections. In the change map obtained with the similarity measure, we observe that most of the changes are missed. In this case, 3 vehicles among 25 are missed using the log–ratio thresholding, whereas 17 are missed using the similarity measure.

We present in Fig. 13 a second change detection example performed over a container area in Sendai Harbor (Japan). The two considered images are TerraSAR-X descending Stripmap products acquired respectively on 06/05/2011 and 08/06/2011. These data were provided by the DLR and Astrium GEO–Information Services for research purposes on the Sendai Earthquake event on 11/03/2011. The amplitude images were not filtered before the change detection. The visible changes between the two dates are due to the displacements of containers or cars on the docks (see circled areas 1, 2, 3, and 4 in Fig. 13). An appearing boat is also detected (see circled area 5 in Fig. 13), which is not visible on the optical image because of the different acquisition dates. We observe that many changes occurred between the two acquisitions and that they are all well detected using the MIMOSA method. We also observe a very low number of false detections in the water and over the docks. In this example, the MIMOSA method produces good results even if many changes occur between the acquisitions ($\approx$10% of the pixels in the image are detected as changes).

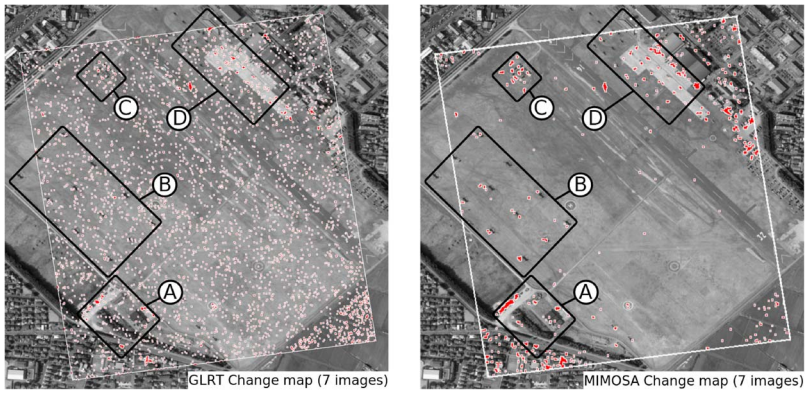

Fig. 14. Orthorectified change detection results between seven images, superimposed to an optical image (Google Earth), where the detected changes are represented in red. (Left) GLRT method (ratio between arithmetic and geometric temporal means thresholded by 1.6; this value is manually selected). (Right) MIMOSA method. Areas A and C illustrate parked vehicles. Area B illustrates large parked helicopters, whereas area D illustrates smaller parked helicopters. The limits of the change detection area are indicated with the white rectangle. A white border is added to the red points to increase readability, the change detection results are not filtered, and no false detection has been removed during orthorectification.

B. Change Detection in a Time Series

In this section, we present the change detection results obtained with MIMOSA method over a time series of seven ascending Stripmap TerraSAR-X images acquired over an airbase in Sendai (Japan). The airbase was not impacted by the effects of the 11/03/2011 tsunami; the visible changes between the images are due to human activities (e.g., parked vehicles, helicopters, and equipment). The processed data are 512 pixel $\times$ 512 pixel sized and are not spatially filtered.

The seven acquisition dates are respectively 31/03, 11/04, 22/04, 14/05, 25/05, 05/06, and 16/06/2011. During the acquisition of these seven images, many changes occurred. The major locations for changes are represented in Fig. 14.

The change detection result obtained with the MIMOSA method is presented on the right of Fig. 14. This result exhibits a very low number of false alarms compared with the result obtained with the GLRT method (see the left side of Fig. 14), where many false detections occurred in the vegetated areas. The GLRT result is computed by thresholding the ratio between the arithmetic and geometric temporal means of the amplitude time series. The threshold value was manually selected to 1.6 and represents the best visual tradeoff between low number of false detections and high number of true detections. We recall that the GLRT thresholding corresponds to detect as changes the point located over a linear function in the scatterplot between the geometric and arithmetic means. The GLRT threshold represents the slope of the line. Thus, the dense point cluster in the scatterplot is crossed by this change detection line and generates a high number of false detections.

The superposition of the change detection result over an optical image enables precise interpretation. Indeed, every change in the MIMOSA change detection map can be associated to a particular ground feature and can be easily interpreted. We observe that the detected changes fit very well the ground features presented in the four areas A, B, C, and D. Moreover, the changes are well detected, whatever the associated temporal amplitude profile. Indeed, some changes are simply related to one image only among the time series, whereas other changes are very regular.

VI. Conclusion

In this paper, we have described a new change detection method for SAR time series, called MIMOSA. This method can process image pairs or time series as well, with a very low computational cost and without any preprocessing step such as spatial speckle filtering. The method is based on the comparison of two different temporal means, whatever the number of images in the time series. This reduction of the data volume to process is very helpful in the case of long time series. A statistical model is used to predict the shape of the scatterplot between the two considered means in order to detect the pairs of means corresponding to changes, which are located in specific places in the scatterplot.

Very good change detection results were presented between two CARABAS-II images, where concealed targets were appearing in the second image. The change maps revealed every appearing target position and their precise shapes, with a very low FAR. A second change detection result was presented using TerraSAR-X data over a container area in Sendai Harbor (Japan), which also produced very good results despite many changes that occurred between the images. Further tests are being performed in order to evaluate the MIMOSA method over areas where the changes are very intense that they completely modify the image aspect and characteristics. These results will be presented as soon as possible.

Change detection results were also presented using a TerraSAR-X time series of seven images over an airbase in Sendai (Japan), where helicopters and vehicles were moved between the acquisitions. Once again, the results are very good since every detected change could have been associated to a ground feature using an optical image. Moreover, the changes are well detected even if they are marginal in the time series. Further tests will be performed using more images in order to validate the MIMOSA method with long time series since the seven-image time series that was used here for demonstration purpose can be considered as relatively short.

Due to the means, taking into account a new incoming image in the existing archive time series is very easy since the two means previously used can simply be updated using the new incoming image, without processing the whole time series again. Thus, an operational use of the MIMOSA method is possible.

APPENDIX A
SAR AMPLITUDE DISTRIBUTIONS

In this appendix, we express the different distributions used in this paper. First, the Rayleigh–Nakagami distribution of parameters μ and L is expressed as

$$\mathcal{RN}[\mu, L](x) = \left(\frac{L}{\mu^2}\right)^L \frac{2x^{2L-1}}{\Gamma(L)} \exp\left[-\frac{Lx^2}{\mu^2}\right]. \quad (31)$$

The Gamma distribution of parameters μ and L is expressed as

$$\mathcal{G}[\mu, L](x) = \left(\frac{L}{\mu}\right)^L \frac{x^{L-1}}{\Gamma(L)} \exp\left[-\frac{Lx}{\mu}\right]. \quad (32)$$

The inverse Rayleigh–Nakagami distribution of parameters μ and M is expressed as

$$\mathcal{RNI}[\mu, M](x) = \frac{2\left(\frac{\sqrt{M}\mu}{x}\right)^{2M} \exp\left[-\left(\frac{\sqrt{M}\mu}{x}\right)^2\right]}{x\Gamma(M)}. \quad (33)$$

The amplitude Fisher distribution of parameters μ, L, and M is expressed as

$$\mathcal{F}_A[\mu, L, M](x) = \frac{2\Gamma(L+M)}{\Gamma(L)\Gamma(M)} \frac{\sqrt{\frac{L}{M}}\left(\frac{\sqrt{\frac{L}{M}}x}{\mu}\right)^{2L-1}}{\left(1+\left(\frac{\sqrt{\frac{L}{M}}x}{\mu}\right)^2\right)^{L+M}}. \quad (34)$$

APPENDIX B
COMPUTATION OF $p_{12}(x_1, x_2)$

The aim of this appendix is the computation of $p_{12}(x_1, x_2)$ [see (8)] in the case of a Fisher model, which corresponds to the estimation of the following integral:

$$\int_0^{+\infty} \frac{1}{t^2} \mathcal{RN}[1, L]\left(\frac{x_1}{t}\right) \mathcal{RN}[1, L]\left(\frac{x_2}{t}\right) \mathcal{RNI}[\mu, M](t)\, dt. \quad (35)$$

Using the expressions of $\mathcal{RN}$ and $\mathcal{RNI}$ (see Appendix A), the latter expression can be developed as

$$p_{12}(x_1, x_2) = \frac{8(x_1x_2L)^{2L}(\mu^2M)^M}{\Gamma(L)^2\Gamma(M)x_1x_2} \int_0^{+\infty} t^{-B} e^{-\frac{A}{t^2}}\, dt \quad (36)$$

where $B = 2(2L + M) + 1$, and $A = L(x_1^2 + x_2^2) + M\mu^2$. The latter integral can be obtained in [38, eq. (3.478.1), p. 342], according to the following relation:

$$\int_0^{+\infty} t^{-B} e^{-\frac{A}{t^2}}\, dt = \frac{1}{2} A^{\frac{1-B}{2}} \Gamma\left(\frac{B-1}{2}\right). \quad (37)$$

Thus, we can write the following expression:

$$\int_0^{+\infty} t^{-B} e^{-\frac{A}{t^2}}\, dt = \frac{1}{2}\, A^{-(2L+M)} \Gamma(2L + M). \quad (38)$$

Combining (36) and (38), we finally obtain the expression presented in (8), with the same notations.

APPENDIX C
COMPARISON WITH BGDS

The multivariate distributions are defined in [19], whereas the BGDs are applied to change detection in [17] and [18]. Let $p_{12}(x_1, x_2)$ be considered, as defined in (9), in the case of a homogeneous texture pattern ($M \to \infty$). The associated limit is computed using [39, eq. (6.1.46), p. 257] and [39, eq. (4.2.21), p. 70]. Thus, the limit is expressed as

$$\lim_{M\to+\infty} p_{x_1x_2}(x_1, x_2) = \frac{4(x_1x_2)^{2L-1}\left(\frac{L}{\mu^2}\right)^{2L} \exp\left[-\frac{L\left(x_1^2+x_2^2\right)}{\mu^2}\right]}{\Gamma(L)^2}. \quad (39)$$

We identify the latter expression as the product of two Rayleigh–Nakagami distributions [see (31) in Appendix A]

$$\lim_{M\to+\infty} p_{12}(x_1, x_2) = \mathcal{RN}[\mu, L](x_1) \cdot \mathcal{RN}[\mu, L](x_2). \quad (40)$$

Let two new random variables X_1 and X_2 be considered respectively corresponding to x_1^2 and x_2^2. After a variable change using a Jacobian operator, we obtain

$$p_{X,12}(X_1, X_2) = \frac{p_{12}(\sqrt{X_1}, \sqrt{X_2})}{|4\sqrt{X_1X_2}|}. \quad (41)$$

Thus, we transform expression (39) from the amplitude to the intensity domain

$$\lim_{M\to+\infty} p_{X,12}(X_1, X_2) = \frac{(X_1X_2)^{L-1}\left(\frac{L}{\mu^2}\right)^{2L} \exp\left[-\frac{L(X_1+X_2)}{\mu^2}\right]}{\Gamma(L)^2}. \quad (42)$$

Note that the latter expression can be found in [17] and [18] by setting $q = L$ and $p_1 = p_2 = \sqrt{p_{12}} = \mu^2/L$ with respect to the notations of [17] and [18] in the monosensor BGD definition. Moreover, we identify the latter expression as the product of two Gamma distributions [see (32) in Appendix A]

$$\lim_{M\to+\infty} p_{X,12}(X_1, X_2) = \mathcal{G}[\mu^2, L](X_1) \cdot \mathcal{G}[\mu^2, L](X_2). \quad (43)$$

APPENDIX D
QUADRATIC MEAN OF N RAYLEIGH–NAKAGAMI DISTRIBUTIONS

The quadratic mean is a composition of three successive operators: 1) square function; 2) arithmetic mean; and 3) square root. Let X be defined as a random variable following the $\mathcal{RN}[\mu, L]$ distribution. The distribution followed by the square of the samples X^2 is the following Gamma distribution [37]:

$$z \mapsto \mathcal{G}[\mu^2, L](z). \quad (44)$$

The distribution followed by the arithmetic mean of N samples following a Gamma function is also a Gamma function. This property is called the addition theorem. Thus, the distribution followed by the arithmetic means of the N samples X^2 is the following Gamma distribution [37]:

$$z \mapsto \mathcal{G}[\mu^2, NL](z). \quad (45)$$

Let two random variables a and b be considered respectively following the $p_a(x)$ and $p_b(x)$ distributions such as $a = b^\eta$. Thus, p_a and p_b are linked by the following fundamental relation:

$$p_b(x) = \eta x^{\eta-1} p_a(x^\eta). \tag{46}$$

Thus, according to (46), the final square root operator over the arithmetic means of the N samples X^2 leads to the following distribution, which is the distribution of the quadratic mean of N samples following a $\mathcal{RN}[\mu, L]$ distribution:

$$p_{\mathcal{M}_2} : z \mapsto 2z\mathcal{G}[\mu^2, NL](z^2). \tag{47}$$

APPENDIX E
MEIJER G-FUNCTIONS

The Meijer G-functions were proposed by Cornelis Simon Meijer in 1936, as a generalization of the hypergeometric functions [29]. These functions are used in this paper because of their interesting properties about multiplicative operations (such as the computation of the geometric mean) and Mellin convolution [37]. The Meijer G-functions are defined on $\mathbb{R}^+$ and can be expressed as

$$\overline{G}_{p,q}^{m,n}\left(x \left| \begin{matrix} a_1, \ldots, a_n; a_{n+1}, \ldots, a_p \\ b_1, \ldots, b_m; b_{m+1}, \ldots, b_q \end{matrix} \right.\right) = \frac{1}{2i\pi} \int_{c-i\infty}^{c+i\infty} \frac{\prod_{j=1}^{m} \Gamma(b_j - s) \prod_{j=1}^{n} \Gamma(1-a_j+s)}{\prod_{j=m+1}^{q} \Gamma(1-b_j+s) \prod_{j=n+1}^{p} \Gamma(a_j-s)} x^s ds \tag{48}$$

where c should verify existence conditions.

We observe that the Meijer G-functions depend on four series of real parameters, i.e., $(a_1, \ldots, a_n)$, $(a_{n+1}, \ldots, a_p)$, $(b_1, \ldots, b_m)$, and $(b_{m+1}, \ldots, b_q)$, respectively. In this paper, the Meijer G-functions that are used are simpler than the latter expression because less parameter lists are used. Indeed, we use at most two lists among the four possible. We present in (49) and (50) the two simplified expressions corresponding to the notations used in this paper.

First, if a single list $(b_1, \ldots, b_N)$ is used, the Meijer G-functions can be expressed as

$$\overline{G}_{0,N}^{N,0}\left(x \left| \begin{matrix} . & ; & . \\ b_1, \ldots, b_N & ; & . \end{matrix} \right.\right) = \frac{1}{2i\pi} \int_{c-i\infty}^{c+i\infty} \prod_{j=1}^{N} \Gamma(b_j - s) x^s \, ds. \tag{49}$$

Second, if two equal-sized lists $(a_1, \ldots, a_N)$ and $(b_1, \ldots, b_N)$ are used, the Meijer G-functions can be expressed as

$$\overline{G}_{N,N}^{N,N}\left(x \left| \begin{matrix} a_1, \ldots, a_N & ; & . \\ b_1, \ldots, b_N & ; & . \end{matrix} \right.\right) = \frac{1}{2i\pi} \int_{c-i\infty}^{c+i\infty} \prod_{j=1}^{N} \Gamma(b_j - s) \prod_{j=1}^{N} \Gamma(1 - a_j + s) x^s \, ds. \tag{50}$$

The two latter Meijer G-functions can be easily evaluated numerically using standard numerical integration techniques.

ACKNOWLEDGMENT

The authors would like to thank the Department of Radar Systems, Swedish Defense Research Agency (FOI), for the CARABAS-II data distribution and also the DLR and Astrium GEO-Information for the TerraSAR-X data distribution.

REFERENCES

[1] S. Quegan, T. Le Toan, J. J. Yu, F. Ribbes, and N. Floury, "Multitemporal ERS SAR analysis applied to forest mapping," *IEEE Trans. Geosci. Remote Sens.*, vol. 38, no. 2, pp. 741–753, Mar. 2000.

[2] D. Haverkamp and C. Tsatsoulis, "Information fusion for estimation of summer MIZ ice concentration from SAR imagery," *IEEE Trans. Geosci. Remote Sens.*, vol. 37, no. 3, pp. 1278–1291, May 1999.

[3] F. Bovolo and L. Bruzzone, "A split-based approach to unsupervised change detection in large-size multitemporal images: Application to tsunami-damage assessment," *IEEE Trans. Geosci. Remote Sens.*, vol. 45, no. 6, pp. 1658–1670, Jun. 2007.

[4] D. J. Weydahl, "Flood monitoring in Norway using ERS-1 SAR images," in *Proc. IGARSS*, Lincoln, NE, USA, May 1996, vol. 1, pp. 151–153.

[5] D. Brunner, L. Bruzzone, and G. Lemoine, "Change detection for earthquake damage assessment in built-up areas using very high resolution optical and SAR imagery," in *Proc. IEEE IGARSS*, Jul. 2010, pp. 3210–3213.

[6] P. Gamba, F. Dell'Acqua, and G. Lisini, "Change detection of multitemporal SAR data in urban areas combining feature-based and pixel-based techniques," *IEEE Trans. Geosci. Remote Sens.*, vol. 44, no. 10, pp. 2820–2827, Oct. 2006.

[7] F. Bovolo, C. Marin, and L. Bruzzone, "A multilevel approach to change detection for port surveillance with very high resolution SAR images," in *Proc. Multitemp*, Trento, Italy, Jul. 12–14, 2011, pp. 9–12.

[8] M. Preiss and N. J. S. Stacy, "Coherent change detection: Theoretical description and experimental result," Defense Sci. Technol. Org., Edinburgh, Australia, DSTO–TR–1851, 2006.

[9] E. J. M. Rignot and J. van Zyl, "Change detection techniques for ERS-1 SAR data," *IEEE Trans. Geosci. Remote Sens.*, vol. 31, no. 4, pp. 896–906, Jul. 1993.

[10] Y. Bazi, L. Bruzzone, and F. Melgani, "An unsupervised approach based on the generalized Gaussian model to automatic change detection in multitemporal SAR images," *IEEE Trans. Geosci. Remote Sens.*, vol. 43, no. 4, pp. 874–887, Apr. 2005.

[11] F. Bovolo and L. Bruzzone, "A detail-preserving scale-driven approach to change detection in multitemporal SAR images," *IEEE Trans. Geosci. Remote Sens.*, vol. 43, no. 12, pp. 2963–2972, Dec. 2005.

[12] C. Carincotte, S. Derrode, and S. Bourennane, "Unsupervised change detection on SAR images using fuzzy hidden Markov chains," *IEEE Trans. Geosci. Remote Sens.*, vol. 44, no. 2, pp. 432–441, Feb. 2006.

[13] P. Lombardo and C. J. Olivier, "Maximum likelihood approach to the detection of changes between multitemporal SAR images," *Proc. Inst. Elect. Eng.—Radar, Sonar Navig.*, vol. 148, no. 4, pp. 200–210, Aug. 2001.

[14] P. Lombardo and T. M. Pellizerri, "Maximum likelihood signal processing techniques to detect a step pattern of change in multitemporal SAR images," *IEEE Trans. Geosci. Remote Sens.*, vol. 40, no. 4, pp. 853–870, Apr. 2002.

[15] F. Bujor, E. Trouve, L. Valet, J.-M. Nicolas, and J.-P. Rudant, "Application of the log-cumulant to the detection of spatiotemporal discontinuities in multitemporal SAR images," *IEEE Trans. Geosci. Remote Sens.*, vol. 42, no. 10, pp. 2073–2084, Oct. 2004.

[16] J. Inglada and G. Mercier, "A new statistical similarity measure for change detection in multitemporal SAR images and its extension to multiscale change analysis," *IEEE Trans. Geosci. Remote Sens.*, vol. 45, no. 5, pp. 1432–1445, May 2007.

[17] F. Chatelain, J.-Y. Tourneret, J. Inglada, and A. Ferrari, "Bivariate gamma distributions for image registration and change detection," *IEEE Trans. Image Process.*, vol. 16, no. 7, pp. 1796–1806, Jul. 2007.

[18] F. Chatelain, J.-Y. Tourneret, and J. Inglada, "Change detection in multisensor SAR images using bivariate gamma distributions," *IEEE Trans. Image Process.*, vol. 17, no. 3, pp. 249–258, Mar. 2008.

[19] S. Kotz, N. Balakrishnan, and N. L. Johnson, *Continuous Multivariate Distributions*, 2nd ed. New York, NY, USA: Wiley, 2000.

[20] L. Alparone, B. Aiazzi, S. Baronti, A. Garzelli, and F. Nencini, "Robust change analysis of SAR data through information-theoretic multitemporal

features," in *Proc. IEEE IGARSS*, Barcelona, Spain, Jul. 23–28, 2007, pp. 3883–3886.
[21] B. Aiazzi, L. Alparone, S. Baronti, A. Garzelli, and C. Zoppetti, "A robust change detection feature for Cosmo-SkyMed detected SAR images," in *Proc. 6th Int. Workshop Anal. Multi-Temp Remote Sens. Images*, Jul. 2011, pp. 125–128.
[22] A. Garzelli, C. Zoppetti, B. Aiazzi, S. Baronti, and L. Alparone, "Robust unsupervised nonparametric change detection of SAR images," in *Proc. IEEE IGARSS*, Jul. 22–27, 2012, pp. 1988–1991.
[23] B. Aiazzi, L. Alparone, and S. Baronti, "Information-theoretic heterogeneity measurement for SAR imagery," *IEEE Trans. Geosci. Remote Sens.*, vol. 43, no. 3, pp. 619–624, Mar. 2004.
[24] G. Quin, B. Pinel-Puyssegur, and J.-M. Nicolas, "Comparison of harmonic, geometric and arithmetic means for change detection in SAR time series," in *Proc. 9th EUSAR Conf.*, Apr. 2012, pp. 255–258.
[25] C. Tison, J.-M. Nicolas, F. Tupin, and H. Maitre, "A new statistical model for Markovian classification of urban areas in high-resolution SAR images," *IEEE Trans. Geosci. Remote Sens.,*, vol. 42, no. 10, pp. 2046–2057, Oct. 2004.
[26] P. S. Bullen, *Handbook of Means and Their Inequalities*. Boston, MA, USA: Kluwer, 2003.
[27] J.-M. Nicolas, A. Maruani, and F. Tupin, "Application of second kind statistics to SAR image processing," in *Proc. EUSAR*, 2002, pp. 685–688.
[28] J.-M. Nicolas, "Introduction aux statistiques de deuxième espèce: Applications des logs-moments et des logs-cumulants à l'analyse des lois d'images radar—Introduction to second kind statistics: Application of log-moments and log-cumulants to SAR image distributions analysis," *Trait. Signal*, vol. 19, no. 3, pp. 139–167, 2002.
[29] H. Bateman, *Higher Transcendental Functions*. New York, NY, USA: McGraw-Hill, 1953.
[30] M. Lundberg, L. M. H. Ulander, W. E. Pierson, and A. Gustavsson, "A challenge problem for detection of targets in foliage," in *Proc. SPIE, Algorithms Synth. Aperture Radar Imagery XIII*, 2006, vol. 6237, p. 62370K.
[31] L. M. H. Ulander, W. E. Pierson, M. Lundberg, P. Follo, P.-O. Frolind, and A. Gustavsson, "Performance of VHF-band SAR change detection for wide-area surveillance of concealed ground targets," in *Proc. SPIE, Algorithms Synth. Aperture Radar Imagery XI*, 2004, vol. 5427, pp. 259–270.
[32] Z. Wei, J. Guan, and J. Wang, "Change detection of concealed targets using repeat–pass SAR images," in *Proc. 1st APSAR*, Nov. 2007, pp. 275–278.
[33] W. Ye, C. Paulson, D. O. Wu, and J. Li, "A target detection scheme for VHFSAR ground surveillance," in *Proc. SPIE, Algorithms Synth. Aperture Radar Imagery XV*, 2008, vol. 6970, pp. 69700Y-1–69700Y-12.
[34] L. Novak, "FOPEN change detection experiments using CARABAS public release data set," in *Proc. SPIE, Algorithms Synth. Aperture Radar Imagery XVII*, 2010, vol. 7699, pp. 76990V-1–76990V-10.
[35] G. Wang, X. Huang, Z. Zhou, and D. An, "A new SAR image change detection algorithm based on texture feature," in *Proc. 3rd Int. APSAR*, Sep. 2011, pp. 1–4.
[36] W. Ye, C. Paulson, and D. Wu, "Target detection for very high-frequency synthetic aperture radar ground surveillance," *IET Comput. Vis.*, no. 2, pp. 101–110, Mar. 2012.
[37] J.-M. Nicolas, "Les distributions de Meijer et leurs propriétés en statistiques de Mellin," Télécom ParisTech, Paris, France, Rapport Telecom Paristech 2011-D002, 2011.
[38] I. S. Gradshteyn and I. M. Ryzhik, *Table of Integrals, Series and Products*, Yu. V. Geronimus and M. Yu. Tseytlin, Eds., 4th ed. New York, NY, USA: Academic, 1965.
[39] M. Abramowitz and I. A. Stegun, *Handbook of Mathematical Functions: With Formulas, Graphs, and Mathematical Tables*. New York, NY, USA: Dover, Jun. 1, 1965.

Guillaume Quin received the engineer degree from the Institut d'Optique Graduate School, École Supérieure d'Optique, Palaiseau, France, in 2010. He is currently working toward the Ph.D. degree in, specializing in SAR permanent scatterer techniques and algorithms for small displacements monitoring at the École Doctorale Informatique, Télécommunication et Électronique, Paris, France.

He is currently with the Commissariat à l'Énergie Atomique et aux Énergies Alternatives (CEA), Direction des Applications Militaires Île-de-France (DAM DIF), Arpajon, France. He has a particular interest in corner reflector design for small displacement measurements. His current research topics involve SAR image statistics and new change detection techniques for SAR time series.

Béatrice Pinel-Puysségur received the engineering degree from the École Nationale Supérieure des Télécommunications (Télécom ParisTech), Paris, France, in 2002; the M.Sc. degree in communications and signal processing from Imperial College London, London, U.K., in 2002; the Master's degree in mathematics from the École Normale Supérieure de Cachan, Cachan, France, in 2003; and the Ph.D. degree from the Institut de Physique du Globe de Paris, Paris, in 2006.

Since 2007, she has been with the Commissariat à l'Énergie Atomique et aux Énergies Alternatives (CEA), Direction des Applications Militaires Île-de-France (DAM DIF), Arpajon, France, where she is currently a Researcher. Her research is focused on SAR interferometry, particularly on atmospheric-effect mitigation, deformation monitoring, and time-series exploitation.

Jean-Marie Nicolas received the Master's degree from the École Normale Supérieure de Saint Cloud, Lyon, France, in 1979 and the Ph.D. degree in physics from the University of Paris XI, Paris, France, in 1982.

He was a Research Scientist with the Laboratoire d'Électronique Philips in medical imaging and then with Thomson-CSF in signal and image processing. He is currently a Professor with the Department of Signal and Image Processing, École Nationale Supérieure des Télécommunications (Télécom ParisTech), Paris. His main research interests concern radar imaging.

Philippe Loreaux received Ph.D. degree in applied mathematics from Université Pierre et Marie Curie, Paris, France, in 1995.

He is currently with the Commissariat à l'Énergie Atomique et aux Énergies Alternatives (CEA), Direction des Applications Militaires Île-de-France (DAM DIF), Arpajon, France. He worked on numerical schemes to solve multiflow partial differential equations to study hydrodynamic instabilities. Then, he was interested in turbulence models using direct numerical simulations on parallel computers. He focused his studies on SAR imagery ten years ago. He is currently specializing in image coregistration techniques, permanent scatterer techniques for time series, and change detection.